

The rate and latency of star formation in dense, massive clumps in the Milky Way [★]

M. Heyer^{1,2}, R. Gutermuth¹, J.S. Urquhart^{2,3}, T. Csengeri², M. Wienen², S. Leurini², K. Menten², and F. Wyrowski²

¹ Department of Astronomy, University of Massachusetts, Lederle Research Building, Amherst, MA 01003
e-mail: heyer@astro.umass.edu

² Max Planck Institute for Radio Astronomy, Auf dem Hügel 69, 53121 Bonn, Germany

³ Centre for Astrophysics and Planetary Science, University of Kent, Canterbury, CT2 7NH, United Kingdom

January 27, 2016

ABSTRACT

Context. Newborn stars form within the localized, high density regions of molecular clouds. The sequence and rate at which stars form in dense clumps and the dependence on local and global environments are key factors in developing descriptions of stellar production in galaxies.

Aims. We seek to observationally constrain the rate and latency of star formation in dense massive clumps that are distributed throughout the Galaxy and to compare these results to proposed prescriptions for stellar production.

Methods. A sample of 24 μ m-based Class I protostars are linked to dust clumps that are embedded within molecular clouds selected from the APEX Telescope Large Area Survey of the Galaxy. We determine the fraction of star-forming clumps, f_* , that imposes a constraint on the latency of star formation in units of a clump's lifetime. Protostellar masses are estimated from models of circumstellar environments of young stellar objects from which star formation rates are derived. Physical properties of the clumps are calculated from 870 μ m dust continuum emission and NH₃ line emission.

Results. Linear correlations are identified between the star formation rate surface density, Σ_{SFR} , and the quantities Σ_{H2}/τ_{ff} and Σ_{H2}/τ_{cross} , suggesting that star formation is regulated at the local scales of molecular clouds. The measured fraction of star forming clumps is 23%. Accounting for star formation within clumps that are excluded from our sample due to 24 μ m saturation, this fraction can be as high as 31%, which is similar to previous results. Dense, massive clumps form primarily low mass ($< 1-2 M_\odot$) stars with emergent 24 μ m fluxes below our sensitivity limit or are incapable of forming any stars for the initial 70% of their lifetimes. The low fraction of star forming clumps in the Galactic center relative to those located in the disk of the Milky Way is verified.

Key words. Stars: formation – Stars:protostars – ISM: clouds – Galaxy: disk

1. Introduction

The formation of young stars and stellar clusters in galaxies follows a sequence of interstellar processes that progressively redistributes gas into denser, more compact configurations. Clouds of primarily molecular gas develop from the diffuse, atomic interstellar medium in response to gravito-magnetic-thermal instabilities within spiral arms or converging flows of warm, neutral material (Kim & Ostriker 2006; Heitsch et al. 2006; Dobbs et al. 2014), or may build-up into larger complexes from the agglomeration of small, pre-existing molecular clouds (Dobbs 2008). Large molecular clouds typically fragment into clumps with enhanced volume and column density that comprise 5-10% of the mass of the cloud (Battisti & Heyer 2014). The clumps break down further into localized parcels of gas (cores) with even higher volume densities (Beuther et al. 2007; Schneider et al. 2015). Single, newborn stars emerge from these localized cores while young stellar clusters are generated if the clump itself is gravitationally unstable (Bate et al. 2003; Vázquez-Semadeni et al. 2009). Understanding how each step in this sequence limits the rate and yield of newborn stars is a key requirement to the development of a complete and predictive description of star formation in galaxies. In this study, we address whether star formation is regulated by global, galaxy-wide processes, or by the local conditions of the gas from which stars condense.

Several recent studies have addressed this issue using data that spans a large range in spatial scales and environmental conditions (Krumholz et al. 2012; Federrath 2013; Salim et al. 2015). Krumholz et al. (2012) analyzed star formation rates and molecular gas properties for molecular clouds in the solar neighborhood, Local group galaxies, unresolved disks, and starburst galaxies in the local and high-redshift universe. With these data, they evaluated several proposed star formation relationships that describe the variation of star formation rates with the amount of gas processed over key timescales, such as the orbital period and free-fall time. The volumetric law, expressed as $\Sigma_{SFR} = \epsilon_{ff} \Sigma_{H2} / \tau_{ff}$, where Σ_{H2} is the molecular gas surface density, τ_{ff} is the free-fall time, and ϵ_{ff} is the star formation efficiency per free-fall time, provided the best fit to the full range of data for $\epsilon_{ff}=0.01$. This value for the efficiency is supported by theoretical estimates (Krumholz & McKee 2005; Padoan et al. 2012).

Evans et al. (2014) examined a more recent compilation of young stellar objects within the Gould's Belt star forming regions. They identified a linear relationship between the star formation rate and the amount of dense gas mass that is consistent with a threshold for star formation, $\Sigma_{SFR} = f_{dense} \Sigma_{H2} / \tau_{dense}$, where f_{dense} is the fraction of dense gas within a molecular cloud, and τ_{dense} is a characteristic timescale for this dense gas. Moreover, they found no correlation between the star formation rate

and mass for cloud extinctions greater than 2 magnitudes and no correspondence with the volumetric law.

In this study, we investigate the star formation rates and gas properties of high density clumps embedded within molecular clouds distributed throughout the Milky Way. These data extend the number and environment of resolved, Galactic star forming regions with which to evaluate the star formation laws. The ratio of star forming to quiescent clumps is determined to estimate the time required for a typical clump to initiate star formation.

2. Data and source selection

We exploit the information within two surveys of the Galactic plane – the APEX Telescope Large Area Survey of the Galaxy, (ATLASGAL) (Schuller et al. 2009; Csengeri et al. 2014) and the Spitzer MIPS GAL survey of $24\mu\text{m}$ emission (Carey et al. 2009). These surveys respectively trace the location and properties of dense clumps and color-selected young stellar objects in the Milky Way. ATLASGAL imaged the $870\mu\text{m}$ thermal dust continuum emission over longitudes $60^\circ > l > 280^\circ$ and latitudes $|b| < 1.5^\circ$ with more extended latitude coverage, $-2 < b < +1$ between 280° and 300° . The angular resolution of the survey is $19.2''$ and the surface brightness sensitivity is typically 70 mJy/beam . Two source catalogs have been constructed from the ATLASGAL image data. Csengeri et al. (2014) tabulated a list of compact objects based on the Gaussclump decomposition algorithm which samples localized emission peaks (Stutzki & Guesten 1990). Urquhart et al. (2014a) applied the SExtractor algorithm to define spatially connected structures (Bertin & Arnouts 1996). Such objects are generally more extended and circumscribe the localized emission peaks. In this study, we use the Urquhart et al. (2014a) catalog, which includes a set of mask images that define the set of pixels tagged to each ATLASGAL source.

The MIPS GAL Survey is a Legacy Program of the Spitzer Space Telescope that imaged the 24 and $70\mu\text{m}$ emission along the Galactic plane over the areas $-68^\circ < l < 69^\circ$, $|b| < 1^\circ$ and $-8^\circ < l < 9^\circ$, $|b| < 3^\circ$ to a sensitivity depth of 1 mJy (Carey et al. 2009). Gutermuth & Heyer (2015) constructed a $24\mu\text{m}$ point source catalog from the MIPS GAL images as well as a lower signal to noise archive set of point sources. Here, we restrict our analysis to the more reliable set of catalog sources. Owing to limited sensitivity in the MIPS detectors, the catalog does not include $70\mu\text{m}$ photometry. An auxiliary data product of the MIPS GAL source catalog used in this study is the set of differential completeness decay data cubes for each image tile that tabulate the point source detection completeness within 1 arcmin^2 pixels as functions of flux and position given the local background (Gutermuth & Heyer 2015).

2.1. Selecting ATLASGAL sources

We examine dust sources (hereafter, clumps) from ATLASGAL within the Galactic longitudes $60^\circ > l > 300^\circ$ and latitudes, $|b| < 1^\circ$. There are 9494 ATLASGAL sources located within these boundaries.

The effects of saturation and a spatially varying background within the MIPS GAL images must be considered when evaluating star formation activity within a clump. Depending on the local background level, the Mips $24\mu\text{m}$ detectors saturate for points sources with flux $\sim > 2 \text{ Jy}$. The MIPS GAL source catalog constructed by Gutermuth & Heyer (2015) excludes such positions from analysis and flags these locations within the differential completeness decay data cubes. Any ATLASGAL clump

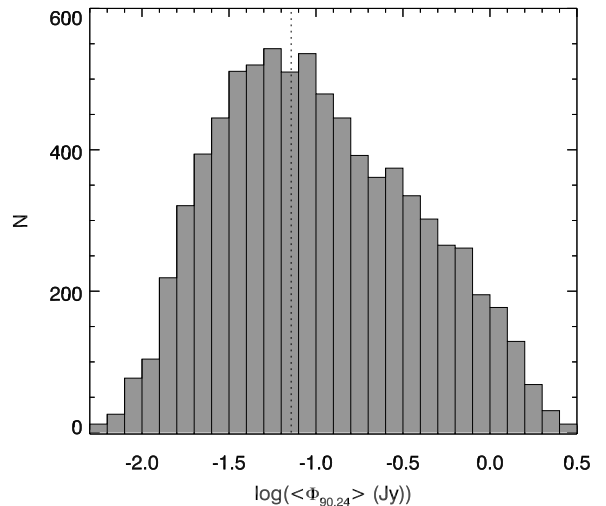


Fig. 1. Distribution of $\langle \Phi_{24,90} \rangle$ values for ATLASGAL clumps with $|b| < 1^\circ$ and containing no saturated pixels at $24\mu\text{m}$. The vertical dotted line marks the maximum value of $\langle \Phi_{24,90} \rangle$ that defines the clump sample and reflects the flux at which the MIPS GAL source catalog is at least 90% complete in these areas.

whose solid angle subtends any flagged, saturated MIPS GAL pixel is excluded from our analysis. Of the original sample of 9494 ATLASGAL clumps, 1487 overlap with saturated MIPS GAL pixels and are removed from the clump list.

The second consideration in our selection of ATLASGAL clumps is source completeness. The $24\mu\text{m}$ background measured by MIPS GAL exhibits large spatial variations throughout the Galactic plane. This variation arises from extended nebulosity excited by ultraviolet radiation that heats interstellar dust grains, which cool by reradiating this energy in the mid and far infrared wavelength bands. The effect of this background is to reduce the local sensitivity to faint $24\mu\text{m}$ point sources. As ATLASGAL clumps can be embedded within such nebulosity, the corresponding sensitivity to associated YSOs within the projected clump area is variable across the Galactic plane. To characterize the $24\mu\text{m}$ background within an ATLASGAL clump and the sensitivity to point sources within its area, we define

$$\langle \phi_{24,90} \rangle = \frac{\int \phi_{24,90} d\Omega}{\int d\Omega}, \quad (1)$$

where $\phi_{24,90}$ is the interpolated value from the differential completeness decay cubes to 90% and the integral is over the solid angle of the ATLASGAL source. Figure 1 shows the distribution of $\langle \phi_{24,90} \rangle$ for 8007 ATLASGAL clumps without $24\mu\text{m}$ saturation. To establish a base sensitivity to YSOs for all ATLASGAL clumps, a source completeness requirement is imposed such that $\langle \phi_{24,90} \rangle$ is less than 72 mJy ($[24]=5$). This limit enables our analysis to be at least 90% complete to protostars with mass greater than $2 M_\odot$ at a distance of 3.9 kpc (see Section 4). A total of 3494 ATLASGAL sources satisfy this requirement and comprise our final sample of clumps.

2.2. Selecting young stellar objects from MIPS GAL

The Gutermuth & Heyer (2015) MIPS GAL source catalog is a compilation of point sources extracted from $24\mu\text{m}$ image product. In addition to the positional centroids, $24\mu\text{m}$ photometry,

and quality flags, the table also includes photometry from the nearest entry in the 2MASS, GLIMPSE, and WISE catalogs if the source positions from these catalogs fall within $2''$ of the MIPS GAL positional centroid. The availability of source fluxes from the near to mid-infrared bands allows one to identify candidate young stellar objects based on the shape of the spectral energy distribution between $1\text{--}25\mu\text{m}$. In this study, we are interested in the early stage YSOs that should still be located within the clumps from which they formed. Such early stage YSOs exhibit rising spectral energy distributions through the mid-IR bands (Class I) (Lada & Adams 1992).

Using the infrared color criteria for Class I or deeply embedded protostars described by Gutermuth *et al.* (2009), 13406 candidate early-stage YSOs are selected from the MIPS GAL catalog with $|l| < 60$ and $|b| < 1$. A fraction of these candidate YSO sources could be AGB stars, which exhibit similar colors as early stage YSOs. Robitaille *et al.* (2008) estimated 30-50% of the GLIMPSE-based red sources are AGB stars and proposed a magnitude and color threshold to distinguish between AGB stars and YSOs. In this study, we do not directly apply this color-magnitude cut since we are interested in the angular coincidence between ATLAS GAL clumps and YSOs. It is possible, yet unlikely, that AGB stars are aligned with the small area subtended by such clumps. Nevertheless, an examination of the photometry for the selected sources satisfies these magnitude and color requirements.

2.3. Selection biases

To address the biases generated by the respective selection requirements for ATLAS GAL clumps and MIPS GAL YSOs, we compare our ATLAS GAL sample and YSO populations to those used in previous studies. Urquhart *et al.* (2014b) compiled a complete sample of massive star forming clumps in the Galaxy by matching sources within the ATLAS GAL catalog to various tracers of massive star formation. These tracers include the Red MSX Source (RMS) Survey (Lumsden *et al.* 2013), the Methonal Multibeam (MMB) Survey (Green *et al.* 2009), and compact HII regions extracted from the Cornish Survey (Purcell *et al.* 2013). Cross linking our sample of 3494 ATLAS GAL clumps with those associated with these signatures of massive star formation, we find the following matched fractions: 23/329 (7%) to RMS, 63/529 (12%) to MMB, and 21/556 (4%) to compact HII regions. The low overlap fraction arises from both saturation within the MIPS GAL images and bright backgrounds in the vicinity of massive stars. Specifically, 43%, 42%, and 58% of the ATLAS GAL sources examined by Urquhart *et al.* (2014b) are discarded in our study due to saturated pixels at $24\mu\text{m}$ for RMS, MMB, and compact HII regions respectively. Similarly, 50%, 46%, and 38% are removed from our sample of clumps owing to the source completeness requirement. The requirements imposed on our sample of ATLAS GAL clumps introduces a bias that mostly excludes sites of massive star formation as traced by the RMS, MMB, and compact HII region CORNISH catalogs.

Robitaille *et al.* (2008) constructed a list of 18337 red infrared objects based on the color selection $[4.5]\text{--}[8.0] > 1$ for sources with $\sim 6:1$ signal to noise in these bands. These red objects are comprised of unresolved planetary nebulae, AGB stars, YSOs, and background galaxies. Using targeted MIPS GAL $24\mu\text{m}$ photometry on these sources, they further refined their sample of YSOs based on $[4.5] > 7.8$ and $[8.0]\text{--}[24] \geq 2.5$. From these cuts, they estimate a total of 11473 YSOs. Within

this sample, 2184 do not have $24\mu\text{m}$ photometry owing to bright background or local saturation of the Mips detectors.

The candidate YSOs derived from the MIPS GAL catalog are matched to 2744 (23%) of the Glimpse-based YSOs. If we impose the same IRAC selection criteria used by Robitaille *et al.* (2008), only 4318 of the MIPS GAL-based YSOs would have been selected by Robitaille *et al.* (2008). From this subset, 2739 (63%) match the YSO list of Robitaille *et al.* (2008). However, the YSOs identified by Robitaille *et al.* (2008) include both early and intermediate stage systems. We have classified the Robitaille *et al.* (2008) sample using the Gutermuth *et al.* (2009) criteria assuming 10:1 signal to noise ratio in the MIPS GAL fluxes (not tabulated in the Robitaille *et al.* (2008) table). This classification results in 3887 Class I, 39 deeply embedded, and 4193 Class 2 objects. Of the 3926 Class I and deeply embedded set, 59% are matched to the YSO sample in this study. When analyzed self-consistently, there is $\sim 60\%$ overlap between the Class I/embedded MIPS GAL-based sample of YSOs and those of Robitaille *et al.* (2008). A large number (11091) of early stage MIPS GAL YSOs are not matched to the GLIMPSE-based YSO sample. This mismatch suggests that the YSOs keyed on $24\mu\text{m}$ detection represent a different population of YSOs than those defined by Robitaille *et al.* (2008). This population is likely to be more deeply embedded within the dense clump from which it condensed and therefore, represents an earlier stage of YSO evolution.

3. Linking young stellar objects to ATLAS GAL clumps

To evaluate the star formation activity within this sample of clumps, it is necessary to associate early-stage YSOs to ATLAS GAL sources. A candidate YSO is linked to an ATLAS GAL clump if its l, b coordinate lies within the solid angle of the clump as defined by its SExtractor mask. A YSO located just outside of the mask area is not considered to be resident within the clump but may represent a later stage of YSO evolution. More than one YSO may be linked to a single clump. Examples of a star-forming clump and a non star-forming, quiescent clump, in which no YSO is linked, are shown in Figure 2. In many cases, a MIPS GAL point source is coincident with an ATLAS GAL clump but its infrared colors are consistent with a main-sequence star.

The fraction of star-forming clumps, $f_* = N_*/N_T$, is 0.23, where N_* is the number of ATLAS GAL clumps with at least one early-stage YSO and $N_T=3494$, is the total number clumps in the sample. This fraction does not significantly change if the completeness limit requirement is relaxed such that all 8007 ATLAS GAL clumps within the searched area with no saturated pixels are examined. In this case, 22% of the ATLAS GAL clumps are associated with a MIPS GAL YSO. While more star forming clumps are identified within this larger sample, the added ATLAS GAL sources with brighter backgrounds (higher values of $< \Phi_{24,90} >$) preclude detections of fainter YSOs. To maintain a well-defined sample, we only consider the 3494 clumps with the imposed background flux limit.

The offset, Δr , between the YSO position and the position of peak $870\mu\text{m}$ intensity is calculated for each star forming clump. This offset is normalized by the clump radius. The distribution of normalized offsets is strongly peaked between 0 and 0.1 and affirms the early-stage status of YSOs linked to these clumps.

Several previous studies have examined the fraction of star forming ATLAS GAL clumps using other star forming tracers.

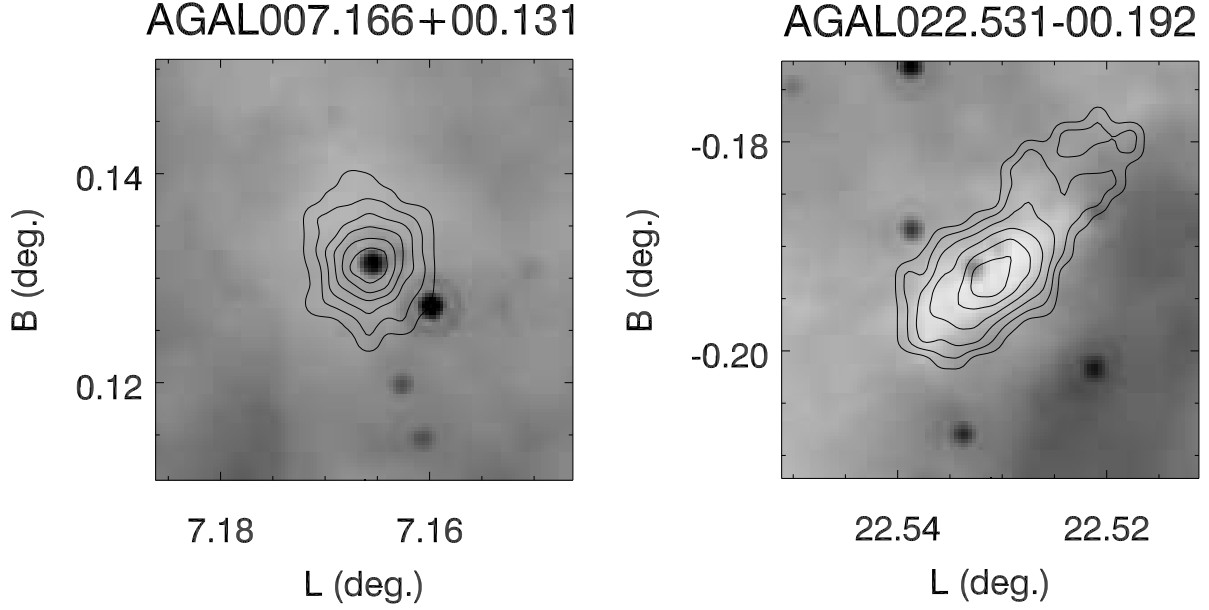


Fig. 2. (left) Star forming ATLASGAL clump, AGAL007.166+00.131, associated with a MIPS GAL selected YSO. The background image is the MIPS GAL 24μm image, the contours show the masked 870μm intensity. The YSO is located at the peak of the dust emission. (right) Quiescent clump, AGAL022.531-00.192. The faint 24μm source projected onto the dust emission is not identified as a YSO.

Contreras et al. (2013) used mid infrared, color-selected data from the MSX mission and found a fraction of star forming clumps of 40% over the longitude range $330 < l < 21$. Csengeri et al. (2014) compiled a list of compact ATLASGAL sources and linked both WISE and MSX based protostars based on angular proximity to the dust peak. They found 30% of the compact clumps were linked to YSOs identified within the WISE source catalog with colors similar to those used in this study and 33% of star-forming clumps when including MSX sources in regions where WISE saturates.

The discrepancy between the fraction of star-forming clumps found in these earlier studies and this MIPS GAL based study, lies primarily in the sample of 1487 ATLASGAL clumps discarded due to saturation in the 24μm band. Figure 3 shows the cumulative distributions of peak and integrated flux densities for ATLASGAL sources with 24μm saturation (dotted line), with bright backgrounds $< \Phi_{24,90} >$ greater than 0.072 Jy (dashed line), and with $< \Phi_{24,90} >$ less than 0.072 Jy (solid line). Clumps with 24μm saturation have larger 870μm peak flux densities than the other groups. Csengeri et al. (2014) demonstrate that clumps with large peak flux densities have a higher probability of being associated with star formation activity. The number of clumps discarded due to saturation that may be linked to YSOs, $N_{*,c}$, is estimated by the integral

$$N_{*,c} = \int P(S_{peak})N(S_{peak})dS_{peak} = 755, \quad (2)$$

where $P(S_{peak})$ is the probability of a star-forming core within bins of the peak flux density (see Figure 18 in Csengeri et al. (2014)). A corrected value for $f_{*,c}$ that accounts for star formation in these saturated zones is $f_{*,c} = \frac{(791+755)}{(3494+1487)} = 0.31$.

This corrected value is more aligned with earlier estimates by Contreras et al. (2013) and Csengeri et al. (2014).

The derived fraction of star forming clumps is a global value over the examined area of the surveys. However, f_* may vary with position in the Galaxy and local environmental conditions. Figure 4 shows the variation of f_* with Galactic longitude. The displayed error-bars reflect the propagation of counting statistics in each bin. The apparent rise of f_* towards both longitude ends of the survey results from the limited number of clumps in these segments and therefore, is not statistically significant. However, the minimum of f_* in the bin centered at $l=2.5^\circ$ is significantly below the other bins. Such reduced star formation activity in this region has been previously recognized (Guesten & Downes 1983; Longmore et al. 2013; Urquhart et al. 2013; Csengeri et al. 2014). Kruijssen et al. (2014) have examined proposed star formation suppressants that could be active within the Central Molecular Zone (CMZ). The primary limitation appears to be a high volume density threshold for star formation ($> 10^7 \text{ cm}^{-3}$) set by the elevated turbulent velocity dispersions in the CMZ (Krumholz & McKee 2005). This threshold is much larger than the mean volume densities of clumps (discussed in §5) located within or near the CMZ.

The local environment of a given clump is expected to have a role in regulating star formation. In particular, regions with higher volume and column density should be more susceptible to forming newborn stars as self-gravity begins to dominate over magnetic and turbulent pressure. Figure 5 show the variation of f_* with 870μm peak flux density and integrated flux. Clumps within the disk and Galactic center ($|l| < 5^\circ$) are shown separately. The corresponding values of H_2 column density are shown in the top axis assuming a dust temperature of 20 K and

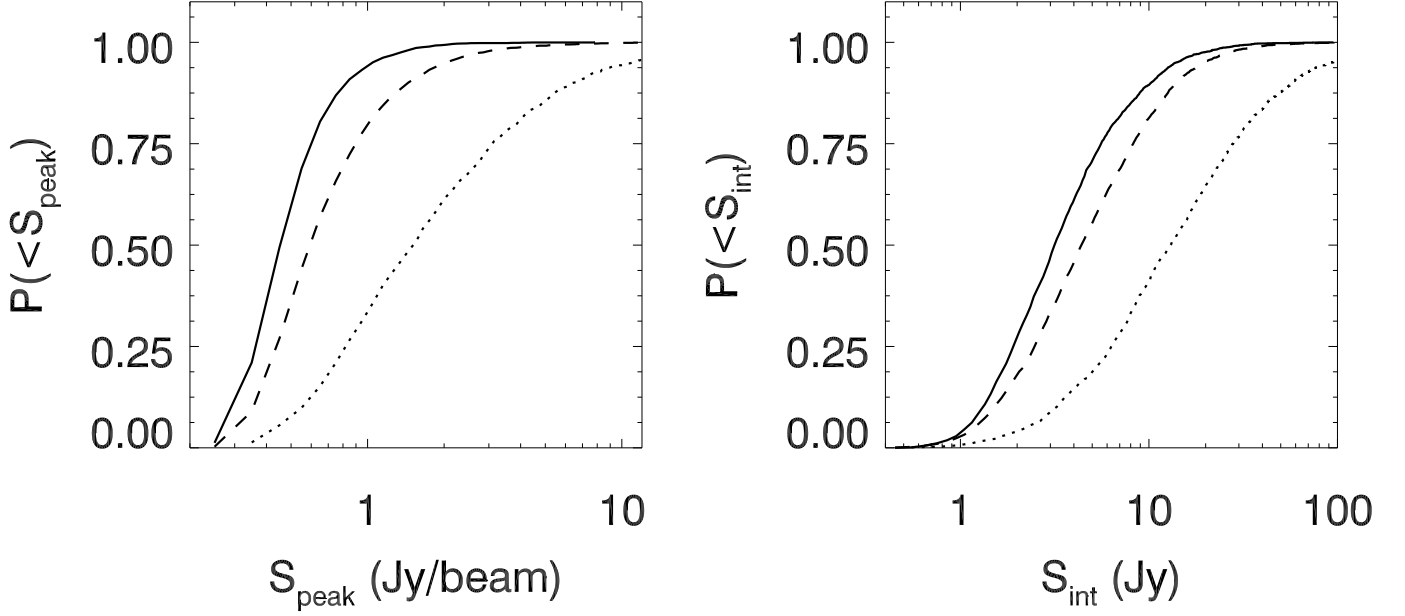


Fig. 3. (left) Cumulative distributions of peak flux intensity of ATLASGAL clumps with MIPSGAL saturation (dotted line), with $\langle \Phi_{24,90} \rangle$ greater than 72 mJy (dashed line) and with $\langle \Phi_{24,90} \rangle$ less than 72 mJy (solid black line). (right) Cumulative distributions of integrated flux density of ATLASGAL clumps for these same groups.

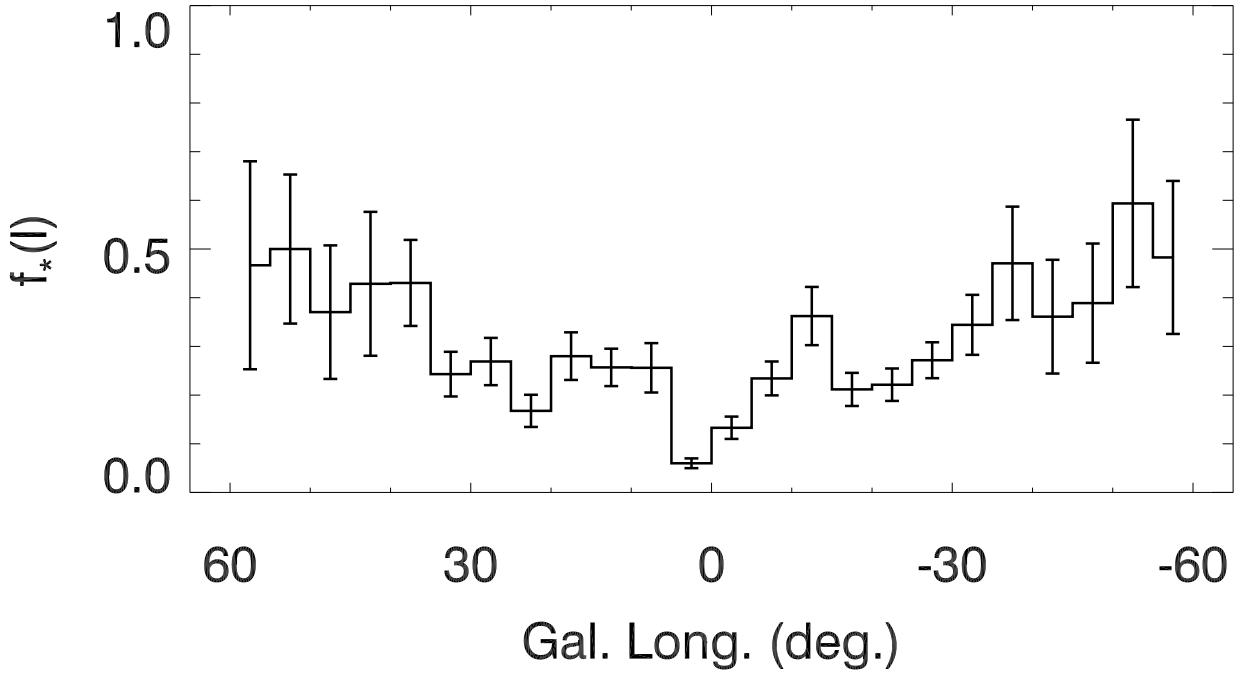


Fig. 4. Fraction of star forming clumps, f_* , with Galactic longitude. The Central Molecular Zone ($|l| < 2.5$) has a significantly smaller fraction of star forming clumps than in the Galactic disk.

dust opacity of $1.85 \text{ cm}^2/\text{gm}$ at $870\mu\text{m}$ (Ossenkopf & Henning 1994) and a gas to dust ratio of 100. Clumps located in the disk show an increasing frequency of star formation with peak flux density. Curiously, no such rise is measured for clumps in the Galactic center region. The fraction of star forming clumps is

constant with integrated flux for both disk and Galactic center clumps

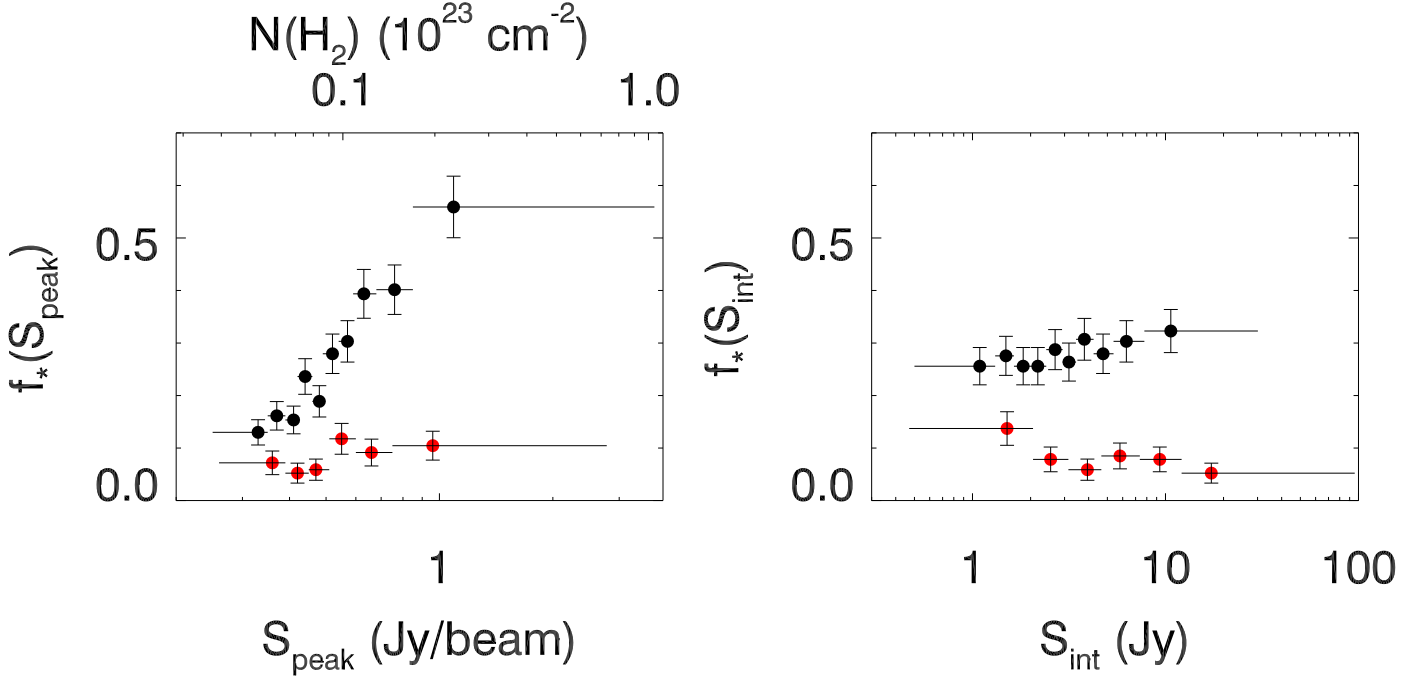


Fig. 5. (left) Variation of f_* with peak flux density and (right) integrated flux for ATLASGAL clumps within the disk (black) and Galactic center (red). The bin sizes are adapted to include equal number of clumps. The horizontal error bars show the bin widths. The vertical error bars reflect the dispersion of values about the mean of the sample. The top x-axis of the left side plot shows the corresponding gas column density assuming a dust temperature of 20 K.

4. MIPS GAL sensitivity to protostellar mass

4.1. Comparison to Robitaille et al. (2006) models

To obtain a better understanding of the candidate protostellar objects identified by MIPS GAL, we have examined the radiative transfer models of YSO environments (central star, disk, envelope) and emergent spectral energy distributions computed by Robitaille et al. (2006). The set of 20,700 models span a range of stellar mass, radius, and surface temperature, accretion rates from the disk and envelope, and different stages of protostellar evolution. For each model, spectral energy distributions are calculated for 10 inclination angles relative to the disk axis. The model SEDs are convolved to commonly used filter response functions to generate broadband fluxes within 50 different sized apertures for each inclination angle at a fixed distance of 1 kpc. In our analysis, we only consider model photometry in the largest aperture of 100,000 AU. Using somewhat smaller apertures ($>20,000$ AU) provided by Robitaille et al. (2006) did not affect our results.

The YSO model broad band fluxes are used to determine early-stage Class I, Class II, and late-stage, Class III objects as applied to the MIPS GAL data in §2.2. Robitaille et al. (2006, 2008) define 3 stages of YSO evolution based on the envelope and disk accretion rates relative to the stellar mass: Stage 1 has $\dot{M}_{\text{env}}/M_* > 10^{-6} \text{ yr}^{-1}$; Stage 2 has $\dot{M}_{\text{env}}/M_* < 10^{-6} \text{ yr}^{-1}$ and $\dot{M}_{\text{disk}}/M_* > 10^{-6}$; Stage 3 has $\dot{M}_{\text{env}}/M_* < 10^{-6} \text{ yr}^{-1}$ and $\dot{M}_{\text{disk}}/M_* < 10^{-6}$. Table 1 shows the number of models in each YSO Stage that are classified as Class I, Class II, and Class III spectral energy distributions. Model YSOs that are classified as Class I objects are primarily linked to Stage 1 YSO models. However, a significant number of Stage 1 model YSOs are classified as Class 2 objects (37%). These Stage 1 models exhibit blue

Table 1. Protostellar stage vs color-based classification of Robitaille et al. (2006) models

	Stage 1	Stage 2	Stage 3
Class I	54253	8055	639
Class II	33940	52225	7804
Class III	72	3399	12784

infrared colors and follow the locus of Stage 2 sources within a plot of IR spectral index and disk accretion rate illustrated in Figure 11 of Robitaille et al. (2006).

The sensitivity of our YSO sample to stellar mass can be partially constrained by examining the distribution of $24\mu\text{m}$ flux density values. Figure 6 shows the run of mean $24\mu\text{m}$ flux with stellar mass for models classified as Class I objects for distances 1, 4.0, and 20 kpc and 2 bins of disk accretion rates: $10^{-9} < \dot{M}_{\text{disk}} < 10^{-7} M_{\odot} \text{ yr}^{-1}$ and $10^{-7} < \dot{M}_{\text{disk}} < 10^{-5} M_{\odot} \text{ yr}^{-1}$. Attenuation of the $24\mu\text{m}$ flux by interstellar dust grains distributed over these distances is not included. Also shown is the distribution of measured $24\mu\text{m}$ fluxes for the full sample of Class I, MIPS GAL YSOs. The models show that fluxes from protostars with masses greater than $12 M_{\odot}$ exceed the 2 Jy saturation limit of the Mips detectors at a distance of 20 kpc. Since this distance is likely an upper limit to any protostar, we assign $12 M_{\odot}$ as an upper protostellar mass limit to which the MIPS GAL catalog is sensitive. The plot also shows that the selected YSO sample is at least 90% complete to protostellar masses of $0.2\text{--}0.4 M_{\odot}$ at a distance of 1 kpc, $1.5\text{--}3 M_{\odot}$ at 4 kpc, and $7 M_{\odot}$ at 20 kpc.

The YSO luminosity can also be used to constrain YSO masses. The emergent bolometric luminosity from a protostellar environment depends on many factors including the disk accre-

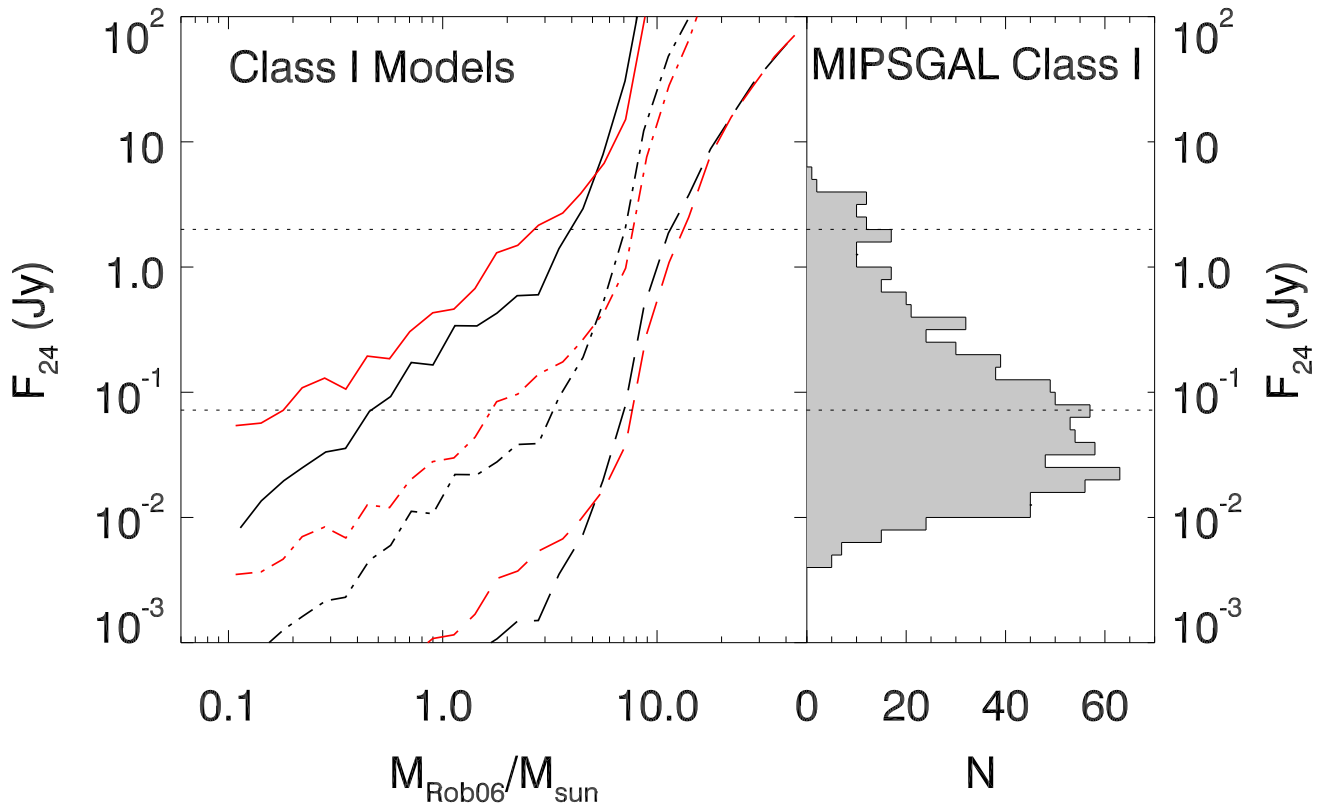


Fig. 6. (left) Variation of mean 24μm flux within bins of protostellar mass and mass accretion rates $10^{-9} \leq \dot{M}_{\text{disk}} < 10^{-7} M_{\odot} \text{yr}^{-1}$ (black) and $10^{-7} \leq \dot{M}_{\text{disk}} < 10^{-5} M_{\odot} \text{yr}^{-1}$ (red) derived from the YSO models of Robitaille *et al.* (2006) and 3 distances (1 kpc (solid line), 4 kpc (dot-dashed lines) and 20 kpc (dashed lines)). (right) Distribution of 24μm fluxes for early stage YSOs linked to ATLASGAL clumps. The upper horizontal dotted line corresponds to the flux level at which the MIPS detectors saturate. The lower horizontal line shows the flux at which MIPSGAL is at least 90% complete for this sample of ATLASGAL clumps.

tion rate and mass of the central, developing star. Consequently, the protostellar luminosity exhibits a large range of values for a given central star mass. A significant fraction of the protostellar bolometric luminosity is emitted at wavelengths longer than 50μm. Since the YSO photometry from the MIPSGAL catalog is limited to wavelengths less than 25μm, we restrict our analysis to the mid-infrared luminosity, L_{IR} , between 2 and 24μm from the available 2MASS, GLIMPSE, and MIPSGAL photometry. Figure 7 shows the variation of L_{IR} , with central, stellar mass, M_{Rob06} , as a 2D-histogram, $\zeta(M, L_{\text{IR}})$, for all models identified as Class I objects with model disk accretion rates in the range, $10^{-8} < \dot{M}_{\text{disk}} < 10^{-5} M_{\odot} \text{yr}^{-1}$ and integrated over all incidence angles. The adopted range of \dot{M}_{disk} is taken from recent observational studies of pre main sequence evolution that derive a comparable range of mass accretion rates for Class I objects (Caratti o Garatti *et al.* 2012; Antonucci *et al.* 2014). For a given central, stellar mass, there is a large spread of L_{IR} values reflecting the varying disk accretion rates and range of model time-steps.

Distances are available for 510 of the ATLASGAL clumps from the study by Wienen *et al.* (2015) or cross-linking ATLASGAL sources with Bolocam Galactic plane dust sources with distances (Ellsworth-Bowers *et al.* 2015). For the Wienen *et al.* (2015) sample, the measured velocity and positions and near/far

side assignment for a given clump were used to derive a distance using the Reid *et al.* (2009) rotation curve. Of this sample, there are 219 star forming clumps which are associated with 290 Class I YSOs. The median distance for all clumps in our sample is 3.9 kpc. The most distant clump is 25.2 kpc.

Infrared luminosities are calculated for star forming clumps with assigned distances. Figure 7 shows the distribution of L_{IR} for these YSOs. The range of observed luminosities matches the mean luminosity values for the stellar masses $< 25 M_{\odot}$. However, at the highest IR luminosities, the expectation value for model central masses is $\sim 7 M_{\odot}$.

4.2. Monte-Carlo estimates to young stellar objects masses

The variation of L_{IR} with stellar mass computed in the Robitaille *et al.* (2006) models and illustrated in Figure 7 enable a statistical estimate to the mass of the YSO object linked to an ATLASGAL clump. For a given star with mid-infrared luminosity, L_{IR} , and luminosity error, $\sigma(L_{\text{IR}})$, a distribution of luminosities, $N(L_*)$, with an expectation value, L_{IR} is created with 16384 elements assuming $\sigma(L_{\text{IR}})$ follows a gaussian distribution. The largest source of luminosity error is due to the distance measurement rather than photometric uncertainties. The fractional distance errors, σ_D/D , for the ATLASGAL sources range from

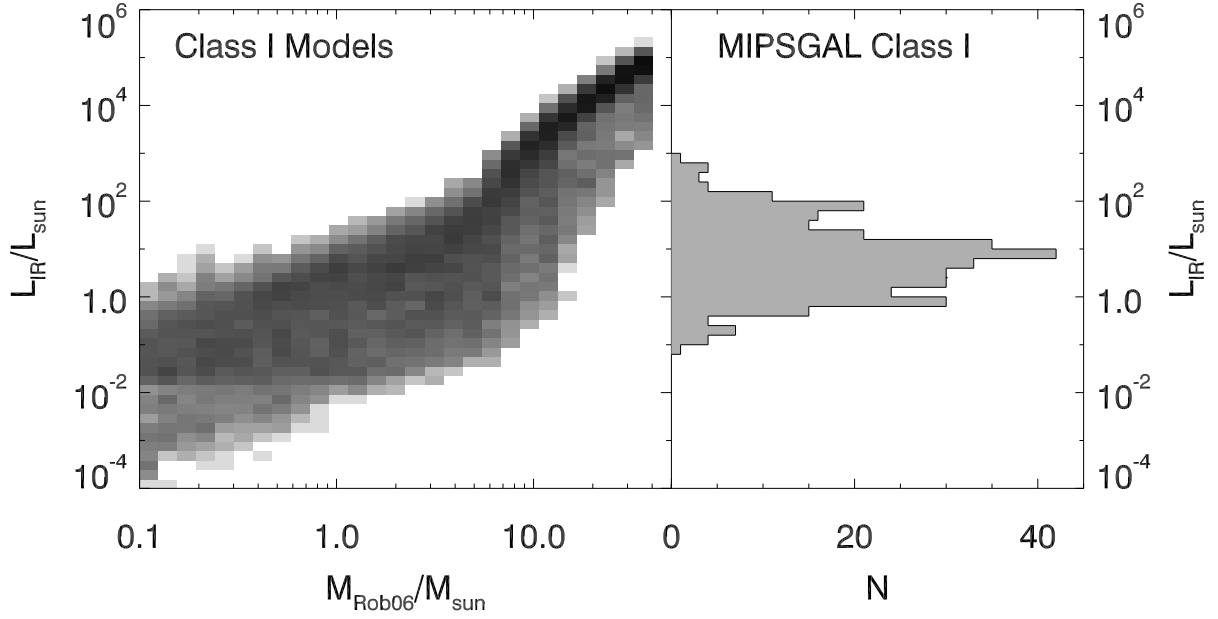


Fig. 7. (left) 2D histogram, $\zeta(M, L_{IR})$, of mass and infrared luminosity for the Robitaille et al. (2006) YSO models with $-8 < \log(\dot{M}_{disk}) < -5$, integrated over all incidence angles and classified as Class I/embedded objects. The color scale is logarithmic and ranges from 0 (white) to 1000 (black) models per bin. (right) Distribution of L_{IR} for 290 Class I, MIPS GAL YSOs linked to 219 ATLASGAL clumps in our sample.

0.1 to 1 (Wienen et al. 2015; Ellsworth-Bowers et al. 2015). The cumulative probability distribution, $P(M, L_{IR}|L_*)$ is constructed from $\zeta(M, L_{IR})$ for this set of Class I models,

$$P(M, L_{IR}|L_*) = \frac{\zeta(< M, L_{IR}|L_*)}{\sum_{M=M_{min}}^{M_{max}} \zeta(M, L_{IR}|L_*)}, \quad (3)$$

where $M_{min}=0.1 M_{\odot}$ and $M_{max}=50 M_{\odot}$ are the minimum and maximum model YSO masses respectively. It describes the fraction of models within mass bins, $M+dM$ for $L_{IR} < L_* < L_{IR}+dL$. For each luminosity value in the distribution, a stellar mass, m_* , is calculated by randomly sampling this cumulative probability distribution. The assigned mass of the star, M_* , is the expectation value of the resultant mass distribution, $N(m_*)$, and YSO mass uncertainties are derived from the shape of $N(m_*)$. The large variance of model luminosity values for a given central, stellar mass arises from the adopted range of disk accretion rates and are reflected in the errors in the derived stellar mass.

To assess the reliability of this Monte Carlo based YSO mass estimate, we apply the method to the Class I model luminosities for various levels of luminosity errors. Figure 8 shows the variation of fractional scatter, $(\langle (M_* - M_{Rob06})^2 \rangle)^{1/2} / M_{Rob06}$ with model YSO mass for both 1% and 100% fractional luminosity errors, where M_* is the Monte-Carlo derived YSO mass and M_{Rob06} is the model central mass. The congruence of these curves demonstrates that the method is limited by the range and diversity of the models that are integrated into $P(M, L_{IR}|L_*)$ rather than distance or photometric errors. For low masses, $0.1 < M_{Rob06}/M_{\odot} < 0.5$, the fractional scatter ranges from 200-750%. For larger masses, the fractional error narrows from 150% at $1 M_{\odot}$ to $\sim 20\%$ at $10 M_{\odot}$. While such fractional errors are too large for many scientific questions, these are sufficient for our

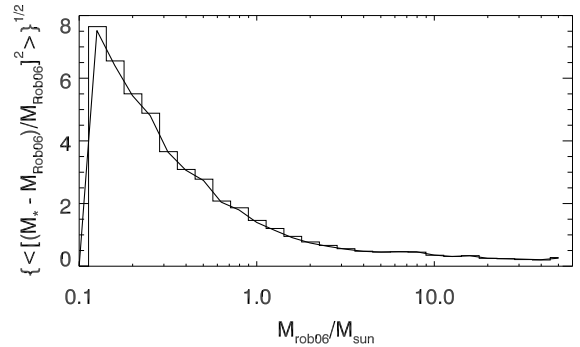


Fig. 8. Variation of normalized scatter within bins of model mass for 1% (histogram) and 100% (solid line) fractional errors in the luminosity. The method is limited by the degeneracy of L_{IR} with a range of central YSO masses rather than observational errors.

more limited goals of defining the efficiency and star formation rate within the sample of dense clumps described in §6.2.

The method is applied to the set of derived infrared luminosities of 290 early-stage MIPS GAL YSOs linked to ATLASGAL sources with established distances. Table 2 tabulates the derived mass and uncertainties for this sample. Also listed are the linked, ATLASGAL source name and infrared luminosity. Figure 9 shows the mass distribution, $dN/d\log M$, for this set of YSOs. Masses range from 1 to $10 M_{\odot}$. An error-weighted fit to the expression $dN/d\log M \propto M^{-\alpha_M}$ for masses greater than $2 M_{\odot}$ produces an index, $\alpha_M = 1.05 \pm 0.14$. The mass distribution is shallower than the high mass IMF functional forms ($\alpha_M \sim 1.3$) of Salpeter (1955) and Kroupa (2001). For the more luminous objects, source confusion of multiple objects within the aperture overpopulates the high mass bins and decreases the

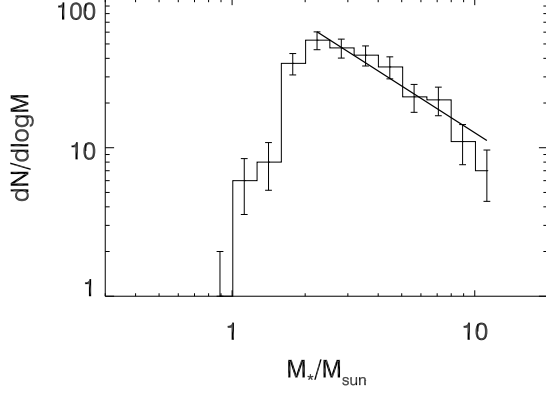


Fig. 9. Mass distribution, $dN/d\log M$, of early stage MIPS GAL YSOs within equal sized logarithmic bins. Error bars reflect counting statistics. The solid line shows the error-weighted fit to the distribution for masses greater than $2 M_\odot$ with index, $\alpha_M = 1.05 \pm 0.14$.

number of objects within the lower mass bins – leading to a shallower slope in the stellar mass distribution. Furthermore, the detected protostar is possibly the brightest and most massive object within a very young cluster developing within the clump. Since the developing cluster is likely in its early stages, it is unlikely that the IMF has been fully sampled and the current most massive YSO could be superceded by a yet to be formed protostar. In any case, the distribution of the maximum protostellar mass, derived from a sample of ATLASGAL sources with a broad range of clump masses, would not necessarily adhere to the established form of the IMF.

Based on the YSO models of Robitaille *et al.* (2006) and our application of the confusion flux limit, it is evident that our list of early-stage newborn stars samples a lower mass population of protostars than those compiled in previous studies. Both Contreras *et al.* (2013) and Urquhart *et al.* (2014b) used low sensitivity MSX IR photometry or established signatures of massive star formation to link newborn stars to ATLASGAL clumps. Csengeri *et al.* (2014) used a combination of MSX and WISE photometry but without the application of a source completeness limit so their sample is biased towards brighter objects and thus, more massive sources or clusters. They adopt a YSO mass range of $8\text{--}10 M_\odot$. MIPS GAL photometry is more sensitive than WISE to fainter YSOs within regions of low background. The smaller sample of ATLASGAL clumps selected by the local $24\mu\text{m}$ background, enables linking fainter YSOs with lower mass while excluding bright YSOs owing to local saturation.

The total stellar mass within a clump, $M_{*,T}$ is the sum of masses of all linked YSOs. For most clumps, only one Class I YSO is identified. Since faint, low mass or highly obscured protostars may also be present within the clump, $M_{*,T}$ is a lower limit to the amount of YSO mass. An upper limit to the total mass of YSOs within the clump can be derived by integrating the 2-component initial mass function (IMF) described by Kroupa (2001).

$$M_{*,\text{imf}} = N_0 \int_{0.1}^{0.5} m^{-\alpha_0+1} dm + N_1 \int_{0.5}^{M_*} m^{-\alpha_1+1} dm, \quad (4)$$

where $\alpha_0 = 1.3$, $\alpha_1 = 2.3$, and M_* is the mass of the largest embedded MIPS GAL YSO within the clump. The constants, N_0, N_1 , are set by M_* and assumes continuity at the intersection of the two power laws such that $N_1 = (M_*)^{\alpha_1}$ and $N_0 =$

$N_1(0.5)^{\alpha_0-\alpha_1} = 2N_1$ stars per mass interval. Since the time scale for Class I protostars is short and the clump masses are small ($<10^4 M_\odot$), it is unlikely that the IMF is fully sampled so $M_{*,\text{imf}}$ is necessarily an upper limit to the amount of protostellar mass. The ratio, $M_{*,\text{imf}}/M_{*,T}$ is listed in Table 3. The derived values can be quite large for $M_* > 4 M_\odot$ but are typically 6–12 for most clumps in our sample.

5. ATLASGAL clump properties

The set of clump properties is compiled for the sub-sample of 219 star forming ATLASGAL sources with measured distances and are fully resolved by the $19''$ beam of the APEX telescope. Clump masses are estimated from the expression

$$M_{cl} = \frac{S_{870} R D^2}{B_{870}(T_D) \kappa_{870}}, \quad (5)$$

where S_{870} is the measured integrated flux density at $870\mu\text{m}$, $B_{870}(T_D)$ is the Planck function evaluated at this wavelength for dust temperature, T_D , assumed to be 20 K, κ_{870} is the dust opacity set to $1.85 \text{ cm}^2/\text{gm}$, R is the gas to dust mass ratio (assumed to be 100) and D is the distance to the source. The clump radius, r_{cl} , is calculated from the effective angular radius, θ_{eff} in radians, $r_{cl} = \theta_{eff} D$. The molecular gas surface density, $\Sigma_{H_2} = M_{cl}/\pi r_{cl}^2$. A mean volume number density is derived assuming a spherical distribution,

$$n_{cl} = \frac{3M_{cl}}{4\pi\mu m_H r_{cl}^3}, \quad (6)$$

where $\mu=2.8$ and m_H is the mass of the hydrogen atom. The free-fall time is $\tau_{ff} = (3\pi/32G\mu m_H n_{cl})^{1/2}$. Finally, the clump crossing time, $\tau_{cross} = 2r_{cl}/\sigma_v$, where σ_v is the NH_3 (1,1) velocity dispersion from Wienen *et al.* (2012) if available. The orbital period of an ATLASGAL source is $\tau_{orb} = 2\pi R_G/V_\theta$, where R_G is the Galactic radius and $V_\theta=254 \text{ km s}^{-1}$ is the azimuthal velocity for a flat rotation curve (Reid *et al.* 2009).

Errors in the time scales, $(\tau_{ff}, \tau_{cross})$, are assumed to be dominated by distance errors, as these relate to the clump density and size respectively. The distance uncertainty to the source dominates the error in the clump mass calculation while the assumptions of constant dust temperature and opacity can lead to additional errors. The distance errors are propagated through the calculations for r_{cl} , n_{cl} , τ_{ff} , and τ_{cross} . The clump properties are listed in Table 3.

6. Discussion

6.1. Latency of star formation in dense clumps

The latency of star formation is the time interval that precedes the formation of stars within a given interstellar volume element. This delay could result from the required development of gravitationally unstable, high density cores within a supersonic, super-Alfvénic medium or the diffusion of the magnetic field to increase local mass to flux ratios. If the volume is already in a state of large-scale gravitational collapse, then this latency period must be very short, $\leq 2\tau_{ff}$.

Assuming a random sampling of the star formation state of a clump over its lifetime, then the measured value of f_* corresponds to the fraction of a clump lifetime, τ_{SF}/τ_{cl} , over which newborn stars are present. Here, τ_{cl} is a average clump lifetime and τ_{SF} is the time over which a clump exhibits evidence for

newborn stars within its domain. If one further assumes that star formation does not go through multiple cycles of star-forming and quiescent stages (Kruijssen & Longmore 2014), then $(1-f_*)$ corresponds to the star formation latency in units of the clump lifetime. This definition for τ_{SF} is different than the definition provided by Mouschovias et al. (2006) who define τ_{SF} as the time period required for the clump or molecular cloud to develop into a state that is susceptible for star formation, which is equivalent to our definition of the star formation latency.

Our analysis of MIPS GAL YSOs and ATLAS GAL clumps determines a rather small value for f_* but one consistent with several previous ATLAS GAL studies (Contreras et al. 2013; Csengeri et al. 2014). Earlier studies connecting embedded protostars from the IRAS Point Source Catalog to dense core regions identified by NH_3 (1,1) or (2,2) line emission, found values of f_* from 33-45% (Beichman et al. 1986; Bourke et al. 1995). Less obscured T Tauri-like YSOs are linked to 1/3 of the dense cores examined by Beichman et al. (1986) indicating that star formation may have started at an earlier stage of the core lifetime.

We can not ignore the possibility that clumps without a MIPS GAL YSO may in fact harbor faint or highly obscured YSOs with fluxes below the local, sensitivity limit. Any conclusions drawn from the value of f_* are limited to a mass range of YSOs for which our YSO list is complete. Based on the turnover of the YSO mass distribution shown in Figure 9 this subsample of 219 clumps is $\sim 90\%$ complete for protostars within the mass range $2 < M_*/M_\odot < 12$. The measured fraction of star forming clumps, corrected for star formation in regions of $24\mu\text{m}$ saturation, is 0.31. Statistically, this sample of ATLAS GAL clumps is engaged in star formation in this stellar mass range for only $\sim 1/3$ of their lifetimes. By complement, such clumps reside within a quiescent, non-star forming state or a state in which only low mass ($< 2M_\odot$) stars are generated for 2/3 of their lifetimes. Ginsburg et al. (2012) demonstrate that the starless phase of clumps forming massive star clusters is very short. Such star and cluster forming clumps are likely excluded from our sample owing to the local $24\mu\text{m}$ background and non-saturation requirements.

Recent numerical simulations of cloud formation and evolution illustrate clouds, clumps, and filaments in a state of hierarchical collapse (Vázquez-Semadeni et al. 2009; Ballesteros-Paredes et al. 2011). In this picture, the production of newborn stars begins very early within dense substructures so most or all clumps with high density contrast with respect to the cloud should contain one or more recently formed stars within several free-fall times. This leads to large values of f_* and very short latency periods of star formation.

These predictions would appear to be incompatible with measured low values of f_* unless one or more of the following conditions apply. A fraction of the clumps may be transient features that never develop to form stars. Adding these short-lived clumps to the population of clumps that do evolve to form stars violates our assumption of random sampling of clumps with mean lifetime, τ_{cl} , and biases our measure of f_* to lower values. Furthermore, the clump lifetimes themselves could be much smaller than the lifetime of the overlying cloud (Heyer & Dame 2015). If $\tau_{SF} = 2\tau_{ff}$, as implied by rapid star formation descriptions, then the measured value of $f_{*,c}$ implies a mean clump lifetime of $\sim 6.5\tau_{ff}$. Finally, if the earliest stars that form have low mass ($< 2M_\odot$) and therefore, are not detected by MIPS GAL, then f_* is underestimated. Such a skewed YSO mass distribution in the earliest stages of a clump may be an essential requirement for the development of more massive stars (Krumholz & McKee

2008). The low mass stars generated in the initial stages of the clump provide a local heating source to the gas, which suppresses fragmentation and enables the collapse of more massive and dense sub-structures that ultimately form high mass stars.

6.2. ATLAS GAL clumps in the context of star formation laws

The data compiled in the previous sections enable an examination of the proposed star formation laws within the dense gas regime of the ATLAS GAL clumps distributed throughout the Milky Way. Previous studies have considered star forming regions within 1 kpc of the Sun that are limited in number (~ 20) and lie within a sector of the Milky Way where the environmental conditions such as molecular gas surface density and ambient UV radiation field may be very different than the inner Galaxy (Gutermuth et al. 2009; Heiderman et al. 2010; Gutermuth et al. 2011; Lada et al. 2012; Heyer & Dame 2015). The study by Wu et al. (2005) evaluated the relationship between the far infrared luminosity and dense gas, as probed by HCN J=1-0 line emission for a sample of massive dense cores with infrared luminosities between 10^3 and $10^7 L_\odot$, many of which contain ultracompact HII regions, and a smaller sub-sample of lower luminosity objects with molecular outflows. They found a linear correlation between L_{FIR} and L_{HCN} for $L_{FIR} > 10^{4.5}$. In our study, we have a more direct measure of H_2 column density gas distributed within dense, compact configurations. The mean densities listed in Table 3, are lower than the critical density required to excite the HCN J=1-0 line but are generally higher than 10^4 cm^{-3} suggested by Lada et al. (2012) as a threshold for the star formation process to commence. This sample is also larger in number than these previous studies and therefore, offers improved statistics. The primary limitations to our analysis are the inability to detect faint or highly obscured YSOs whose fluxes fall below our completion limit and the large uncertainties in YSO mass extracted from the spectral energy distribution models of Robitaille et al. (2006).

The star formation rate within a star-forming ATLAS GAL clump is estimated from the total mass of associated early stage MIPS GAL YSOs, tabulated in Table 2, divided by the time scale for Class I protostars.

$$\dot{M}_* = \frac{M_{*,T}}{\tau_{SF}} \quad (7)$$

Studies of nearby clouds that are primarily forming low mass stars estimate the age of Class I protostars as 0.5 Myr (Evans et al. 2009; Gutermuth et al. 2009). We adopt this value for all YSO masses. An upper limit to \dot{M}_* is set by replacing $M_{*,T}$ with $M_{*,imf}$ in equation 7. The star formation rate surface density is

$$\Sigma_{SFR} = \frac{\dot{M}_*}{\pi r_{cl}^2} \quad (8)$$

Uncertainties for Σ_{SFR} are propagated from the error in the YSO masses tabulated in Table 3 and distance errors.

To make a fair comparison of derived star formation rates with the extragalactic measurements, it is important to place upper limits to the star formation rates for ATLAS GAL sources that are not linked to a Class I MIPS GAL source (D. Kruijssen, private communication). Such non-star forming structures are included in extragalactic CO or dust measurements of gas column density. For each of the 291 resolved, non star forming clumps with an assigned distance, we calculate a $24\mu\text{m}$ luminosity, L_{24} , based on the adopted $24\mu\text{m}$ completeness limit flux of 72 mJy.

From this luminosity, the same Monte-Carlo method is applied to estimate a corresponding YSO mass and uncertainties using the probability distributions, $P(M, L_{24}|L_*)$ similarly constructed from the Robitaille *et al.* (2006) Class I models. We assign the $+2\sigma$ mass as an upper limit for the YSO mass within each unlinked ATLASGAL clump. The corresponding 2σ upper limits of Σ_{SFR} for these non-star forming clumps are reported in Table 4.

The variation of Σ_{SFR} with H_2 mass surface density, Σ_{H_2} , for these ATLASGAL sources is shown in Figure 10a. The 2σ upper limits for the starless clumps are plotted as crosses. For context, points for local star forming regions from Gutermuth *et al.* (2009), Lada *et al.* (2012), and Evans *et al.* (2014) are plotted. The star formation relationships determined by Kennicutt (1998) and Bigiel *et al.* (2008) for galaxies are also shown. The detected ATLASGAL star formation rates lie well above the extragalactic relationships for the same value of Σ_{H_2} , as found by Heiderman *et al.* (2010) and Gutermuth *et al.* (2011). This displacement is reduced when including the star formation rate upper limits for non star forming clumps and suggests that there is no large discrepancy of star formation rates for comparable gas surface density between resolved star forming regions and the extragalactic measurements.

No significant correlation between Σ_{SFR} and Σ_{H_2} is present in this set of ATLASGAL clumps. For most of these points, there is a limited amount of dynamic range in Σ_{H_2} and the scatter of Σ_{SFR} is large, which precludes the identification of any relationship. Errors in Σ_{SFR} surely contribute to some of this scatter but variance within the clump population is also a source. The cloud of ATLASGAL points and the data from the local star forming regions do align along the proposed linear relationship by Wu *et al.* (2005) (solid line in Figure 10a) that describes the star formation rates in dense gas.

The global star formation law posits that the production of stars is regulated by large scale, radial processes that affect the gas over an orbital time scale (Wyse & Silk 1989; Kennicutt 1998; Tan 2000, 2010; Suwannajak *et al.* 2014). The variation of Σ_{SFR} with Σ_{H_2}/τ_{orb} is shown in Figure 10b. Orbital periods for the solar neighborhood clouds and clumps compiled by Gutermuth *et al.* (2009), Lada *et al.* (2012), and Evans *et al.* (2014) are derived for $R_G=8.4$ kpc (Reid *et al.* 2009). There is no correlation between these quantities within the set of ATLASGAL points owing in part, to the limited range of R_G values. 95% of the star-forming clumps are located between Galactic radii 2 kpc and 8 kpc. The cloud of points is aligned with those of the solar neighborhood clouds along a linear line with $\epsilon_{orb}\sim 1$. This efficiency value is much larger than the value of ~ 0.1 estimated by Kennicutt (1998) for disk galaxies. While large scale processes may impact the formation of molecular clouds from the diffuse, atomic medium (Koda *et al.* 2015), these do not impact the star formation rates within the dense clumps of molecular clouds.

The volumetric star formation law considers a fixed fraction of a molecular cloud or clump, ϵ_{ff} , is converted into stars over a free-fall time based on the local volume density. Figure 10c shows the ATLASGAL star forming regions in context with the volumetric law. An error-weighted fit to the ATLASGAL points shows a linear relationship with normalization $\epsilon_{ff} = 0.003 \pm 0.001$, a power-law index 1.02 ± 0.06 , a reduced $\chi^2=0.89$, and a root mean square of 0.4 dex. The fitted value for ϵ_{ff} is ~ 3 -4 times lower than the value of 0.01 found by Krumholz *et al.* (2012) that describes star formation rates from local clouds to high redshift galaxies. We emphasize that these star formation rates are lower limits. Repeating the fit using the

total YSO mass assuming a fully sampled IMF, the parameters are: $\epsilon_{ff} = 0.02 \pm 0.01$, a power-law index 1.14 ± 0.06 , a reduced $\chi^2=1.2$, and a root mean square of 0.5 dex. Since $\Sigma_{SFR,imf}$ is an upper limit, the true value of ϵ_{ff} lies somewhere between these two (0.003, 0.02) values. On the other hand, inclusion of the 2σ upper limits for non-star forming clumps would bias the efficiency towards lower values.

Elmegreen (2000) summarizes observations that suggest star formation in dense structures is rapid. The production of new stars begins immediately after the structure has condensed from its overlying substrate and is completed within several crossing time scales. The dependence of the star formation rate on the crossing time scale within this set of ATLASGAL clumps is examined in Figure 10d. There are 59 star forming and 44 non-star forming ATLASGAL clumps with velocity dispersions from NH_3 line emission that also satisfy the $24\mu m$ completeness and resolved clump size requirements. The star formation rate surface density, Σ_{SFR} is well correlated with $\Sigma_{H_2}/\tau_{cross}$. An error-weighted power law fit to the 59 points produces the following parameters: $\epsilon_{cross} = 0.03 \pm 0.016$, a power-law index 0.91 ± 0.09 , a reduced $\chi^2=3.2$, and a root mean square of 0.3 dex. While this is a lower limit to the efficiency of star forming clumps per crossing time, inclusion of the upper limits of non-star forming clumps would lower the overall efficiency within dense substructures of molecular clouds. Based on these data, star formation is well linked to the local crossing time of a clump but does not proceed rapidly or efficiently.

Overall, the derived star formation rates within dense clumps traced by the thermal dust continuum emission favors the regulation of stellar production by local conditions or processes. The strongest correlations are identified in Figures 10c,d in which Σ_{SFR} depends on the dense, gas surface density normalized by the free-fall and clump crossing times respectively. The low efficiencies of 1% or less for ϵ_{ff} and ϵ_{cross} and the long latency times implied by f_* , point towards a localized process or state that slows the rate of star formation or limits the amount of material that is transformed into stars within these dense gas configurations.

7. Conclusions

We have examined the ATLASGAL and MIPS GAL source catalogs to link Class I young stellar objects to their natal, massive, dense clump from which these formed. Only 23% of the 3494 clumps, selected to have low, $24\mu m$ backgrounds, are found to be associated with early-stage protostars. Accounting for clumps with saturated $24\mu m$ emission, this fraction increases to 31%. Using models of YSO circumstellar environments, we estimate the central masses of YSOs linked to ATLASGAL sources with assigned distances. The YSO mass range is 1 to $10 M_\odot$, limited on the low side by background and on the high side by saturation of the Mips $24\mu m$ detectors. Star formation rates are derived for ATLASGAL sources with distances as well as upper limits for starless clumps. These are compared to star formation regions in the solar neighborhood and extragalactic relationships. Star formation relationships that consider local gas conditions such as the free-fall and crossing times provide a reasonable description to this set of resolved star forming regions.

Acknowledgements. This work was supported by the NASA ADAP grant NNX13AF08G (MH,RG), the Collaborative Research Center 956, funded by the *Deutsche Forschungsgemeinschaft, DFG* via the SPP (priority program) (MH) and the *Deutsche Forschungsgemeinschaft, DFG* via the SPP (priority program) 1573 'Physics of the ISM' (TCs). The authors thank the referee for insightful

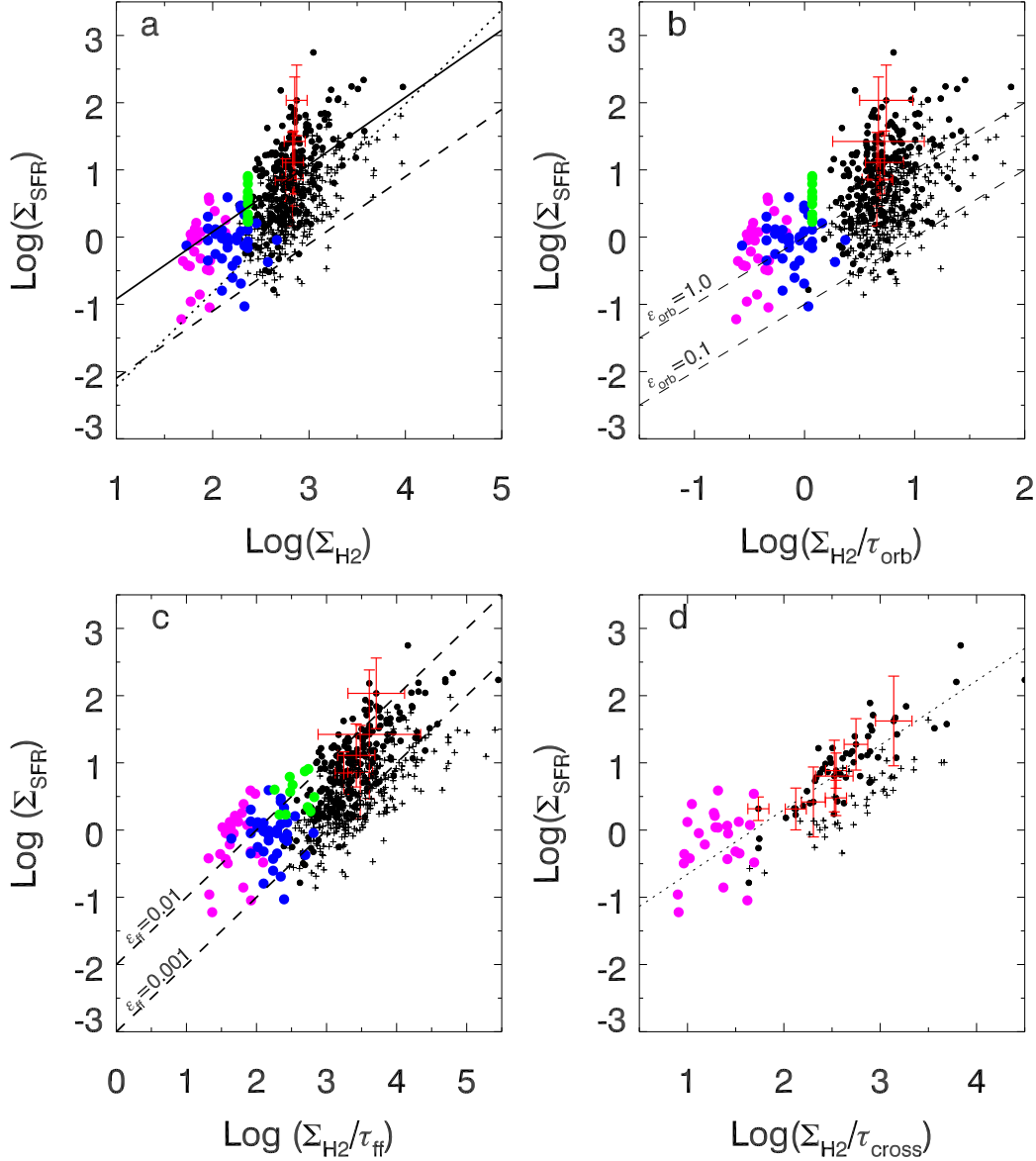


Fig. 10. Variation of star formation rate normalized by area, Σ_{SFR} with a) Σ_{H2} , b) Σ_{H2}/τ_{orb} , c) Σ_{H2}/τ_{ff} , and d) Σ_{H2}/τ_{cross} for resolved ATLASGAL clumps with measured distances. Points correspond to star forming ATLASGAL clumps (black circles and red error bars), 2σ upper limits to Σ_{SFR} for non-star forming ATLASGAL clumps (black crosses) Lada et al. (2012) (green), Evans et al. (2014) (magenta), and Gutermuth et al. (2009) (blue). As discussed in the text, the black circles are lower limits to the true star formation rates. In a) the lines correspond to Kennicutt (1998) (dotted), Bigiel et al. (2008) (dashed), Wu et al. (2005) (solid). In b) and c), the dashed lines correspond respectively to the global star formation law with $\epsilon_{orb}=0.1$ and 1.0 and the volumetric star formation law with $\epsilon_{ff}=0.001$ and 0.01. d), the dotted line is an error-weighted fit to the star forming ATLASGAL clumps.

comments. We acknowledge useful discussions with G. Wilson, D. Kruijssen, and E. Vázquez-Semadeni.

References

- Antoniucci, S., García López, R., Nisini, B., et al. 2014, A&A, 572, A62
 Ballesteros-Paredes, J., Hartmann, L. W., Vázquez-Semadeni, E., Heitsch, F., & Zamora-Avilés, M. A. 2011, MNRAS, 411, 65
 Bate, M. R., Bonnell, I. A., & Bromm, V. 2003, MNRAS, 339, 577
 Battisti, A. J. & Heyer, M. H. 2014, ApJ, 780, 173
 Beichman, C. A., Myers, P. C., Emerson, J. P., et al. 1986, ApJ, 307, 337
 Bertin, E. & Arnouts, S. 1996, A&AS, 117, 393
 Beuther, H., Leurini, S., Schilke, P., et al. 2007, A&A, 466, 1065
 Bigiel, F., Leroy, A., Walter, F., et al. 2008, AJ, 136, 2846
 Bourke, T. L., Hyland, A. R., & Robinson, G. 1995, MNRAS, 276, 1052
 Caratti o Garatti, A., Garcia Lopez, R., Antonucci, S., et al. 2012, A&A, 538, A64
 Carey, S. J., Noriega-Crespo, A., Mizuno, D. R., et al. 2009, PASP, 121, 76
 Contreras, Y., Schuller, F., Urquhart, J. S., et al. 2013, A&A, 549, A45
 Csengeri, T., Urquhart, J. S., Schuller, F., et al. 2014, A&A, 565, A75
 Dobbs, C. L. 2008, MNRAS, 391, 844
 Dobbs, C. L., Krumholz, M. R., Ballesteros-Paredes, J., et al. 2014, Protostars and Planets VI, 3
 Ellsworth-Bowers, T. P., Rosolowsky, E., Glenn, J., et al. 2015, ApJ, 799, 29
 Elmegreen, B. G. 2000, ApJ, 530, 277
 Evans, II, N. J., Dunham, M. M., Jørgensen, J. K., et al. 2009, ApJS, 181, 321
 Evans, II, N. J., Heiderman, A., & Vutisalchavakul, N. 2014, ApJ, 782, 114
 Federrath, C. 2013, MNRAS, 436, 3167

- Ginsburg, A., Bressert, E., Bally, J., & Battersby, C. 2012, *ApJ*, 758, L29
- Green, J. A., Caswell, J. L., Fuller, G. A., et al. 2009, *MNRAS*, 392, 783
- Guesten, R. & Downes, D. 1983, *A&A*, 117, 343
- Gutermuth, R. A. & Heyer, M. 2015, *AJ*, 149, 64
- Gutermuth, R. A., Megeath, S. T., Myers, P. C., et al. 2009, *ApJS*, 184, 18
- Gutermuth, R. A., Pipher, J. L., Megeath, S. T., et al. 2011, *ApJ*, 739, 84
- Heiderman, A., Evans, II, N. J., Allen, L. E., Huard, T., & Heyer, M. 2010, *ApJ*, 723, 1019
- Heitsch, F., Slyz, A. D., Devriendt, J. E. G., Hartmann, L. W., & Burkert, A. 2006, *ApJ*, 648, 1052
- Heyer, M. & Dame, T. M. 2015, *ARA&A*, 53, 583
- Kennicutt, Jr., R. C. 1998, *ApJ*, 498, 541
- Kim, W.-T. & Ostriker, E. C. 2006, *ApJ*, 646, 213
- Koda, J., Scoville, N., & Heyer, M. 2015, *ApJ*
- Kroupa, P. 2001, *MNRAS*, 322, 231
- Kruijssen, J. M. D. & Longmore, S. N. 2014, *MNRAS*, 439, 3239
- Kruijssen, J. M. D., Longmore, S. N., Elmegreen, B. G., et al. 2014, *MNRAS*, 440, 3370
- Krumholz, M. R., Dekel, A., & McKee, C. F. 2012, *ApJ*, 745, 69
- Krumholz, M. R. & McKee, C. F. 2005, *ApJ*, 630, 250
- Krumholz, M. R. & McKee, C. F. 2008, *Nature*, 451, 1082
- Lada, C. J. & Adams, F. C. 1992, *ApJ*, 393, 278
- Lada, C. J., Forbrich, J., Lombardi, M., & Alves, J. F. 2012, *ApJ*, 745, 190
- Longmore, S. N., Bally, J., Testi, L., et al. 2013, *MNRAS*, 429, 987
- Lumsden, S. L., Hoare, M. G., Urquhart, J. S., et al. 2013, *ApJS*, 208, 11
- Mouschovias, T. C., Tassis, K., & Kunz, M. W. 2006, *ApJ*, 646, 1043
- Ossenkopf, V. & Henning, T. 1994, *A&A*, 291, 943
- Padoan, P., Haugbølle, T., & Nordlund, Å. 2012, *ApJ*, 759, L27
- Purcell, C. R., Hoare, M. G., Cotton, W. D., et al. 2013, *ApJS*, 205, 1
- Reid, M. J., Menten, K. M., Zheng, X. W., et al. 2009, *ApJ*, 700, 137
- Robitaille, T. P., Meade, M. R., Babler, B. L., et al. 2008, *AJ*, 136, 2413
- Robitaille, T. P., Whitney, B. A., Indebetouw, R., Wood, K., & Denzmore, P. 2006, *ApJS*, 167, 256
- Salim, D. M., Federrath, C., & Kewley, L. J. 2015, *ApJ*, 806, L36
- Salpeter, E. E. 1955, *ApJ*, 121, 161
- Schneider, N., Ossenkopf, V., Csengeri, T., et al. 2015, *A&A*, 575, A79
- Schuller, F., Menten, K. M., Contreras, Y., et al. 2009, *A&A*, 504, 415
- Stutzki, J. & Guesten, R. 1990, *ApJ*, 356, 513
- Suwannajak, C., Tan, J. C., & Leroy, A. K. 2014, *ApJ*, 787, 68
- Tan, J. C. 2000, *ApJ*, 536, 173
- Tan, J. C. 2010, *ApJ*, 710, L88
- Urquhart, J. S., Csengeri, T., Wyrowski, F., et al. 2014a, *A&A*, 568, A41
- Urquhart, J. S., Moore, T. J. T., Csengeri, T., et al. 2014b, *MNRAS*, 443, 1555
- Urquhart, J. S., Moore, T. J. T., Schuller, F., et al. 2013, *MNRAS*, 431, 1752
- Vázquez-Semadeni, E., Gómez, G. C., Jappsen, A.-K., Ballesteros-Paredes, J., & Klessen, R. S. 2009, *ApJ*, 707, 1023
- Wienen, M., Wyrowski, F., Menten, K. M., et al. 2015, *A&A*, 579, A91
- Wienen, M., Wyrowski, F., Schuller, F., et al. 2012, *A&A*, 544, A146
- Wu, J., Evans, II, N. J., Gao, Y., et al. 2005, *ApJ*, 635, L173
- Wyse, R. F. G. & Silk, J. 1989, *ApJ*, 339, 700

Table 2. Model based protostellar mass and errors

MIPSGAL Name	ATLASGAL Name	L_{IR} (L_{\odot})	M_* (M_{\odot})	$M_*(-2\sigma)$ (M_{\odot})	$M_*(-1\sigma)$ (M_{\odot})	$M_*(+1\sigma)$ (M_{\odot})	$M_*(+2\sigma)$ (M_{\odot})
MG005.0424-00.0976	AGAL005.041-00.097	2.78e+00	2.39	0.20	0.50	3.98	10.00
MG005.2041-00.0362	AGAL005.202-00.036	4.04e+01	5.65	1.26	2.51	7.94	15.85
MG005.3946+00.1939	AGAL005.397+00.194	8.12e-01	1.85	0.13	0.25	3.98	7.94
MG005.6181-00.0821	AGAL005.617-00.082	8.58e+01	7.10	2.00	3.98	10.00	15.85
MG007.1654+00.1314	AGAL007.166+00.131	2.09e+01	4.59	1.26	2.00	6.31	12.59
MG007.3349-00.5665	AGAL007.333-00.567	1.02e+01	3.77	0.63	1.26	6.31	12.59
MG007.6351-00.1922	AGAL007.636-00.192	8.35e+01	7.08	2.51	3.98	10.00	15.85
MG008.2032+00.1917	AGAL008.206+00.191	1.80e+00	2.20	0.16	0.40	3.98	10.00
MG008.5486-00.3394	AGAL008.544-00.341	5.95e+00	3.06	0.40	1.00	5.01	12.59
MG008.7038-00.4121	AGAL008.706-00.414	6.71e+00	3.45	0.50	1.00	6.31	12.59
MG008.7081-00.4162	AGAL008.706-00.414	1.41e+01	4.06	0.79	1.58	6.31	12.59
MG008.8033-00.3234	AGAL008.804-00.327	2.51e+00	2.38	0.20	0.50	5.01	10.00
MG008.9392-00.5303	AGAL008.954-00.532	2.01e+01	4.59	1.26	2.00	6.31	12.59
MG008.9555-00.5352	AGAL008.954-00.532	1.45e+01	4.03	0.79	1.58	6.31	12.59
MG008.9565-00.5426	AGAL008.954-00.532	1.72e+01	4.58	1.26	2.00	6.31	12.59
MG009.2826-00.1506	AGAL009.284-00.147	8.99e-01	1.90	0.13	0.32	3.98	7.94
MG009.8474-00.0321	AGAL009.851-00.031	1.33e+01	4.01	0.50	1.26	6.31	12.59
MG009.8572-00.0405	AGAL009.851-00.031	1.50e-01	1.11	0.10	0.16	2.00	5.01
MG009.9667-00.0206	AGAL009.966-00.021	4.71e+01	6.15	2.00	3.16	10.00	15.85
MG010.4082-00.2013	AGAL010.404-00.201	3.01e+00	2.46	0.20	0.50	5.01	10.00

Table 3. Properties of resolved star forming ATLASGAL clumps with distance measure

ATLASGAL Name	D ^a	$\sigma(D)$	Ref.	M(H ₂)	$\sigma(M(H_2))$	Σ_{H_2}	$\sigma(\Sigma_{H_2})$	Σ_{SFR}^b	$\sigma(\Sigma_{SFR})$	$M_{inf}/M_{*,T}$	n_{cl}	τ_{ff}	τ_{orb}	τ_{cross}^c
	(kpc)				(M _⊙)	(M _⊙ pc ⁻²)		(M _⊙ pc ⁻² Myr ⁻¹)			(10 ⁴ cm ⁻³)	(Myr)	(Myr)	(Myr)
AGAL005.041-00.097	2.74	1.35	1	129	128	1037	259	38	55	8	5.72	0.13	133	0.00
AGAL005.202-00.036	2.68	1.34	1	78	77	744	186	108	131	32	4.49	0.15	135	0.00
AGAL005.397+00.194	2.62	1.31	1	142	142	311	78	8	14	5	0.90	0.33	136	1.23
AGAL005.617-00.082	25.15	12.07	1	37030	35543	429	107	0	0	45	0.09	1.03	395	9.90
AGAL007.166+00.131	10.25	0.14	1	2223	60	1274	319	5	4	23	1.88	0.22	51	1.60
AGAL007.333-00.567	3.32	0.75	1	567	256	457	114	6	6	17	0.80	0.34	120	2.10
AGAL007.636-00.192	9.29	0.08	1	1276	21	692	173	8	5	44	0.99	0.31	35	1.99
AGAL008.206+00.191	2.46	1.43	2	90	105	622	155	30	50	7	3.18	0.17	139	0.76
AGAL008.544-00.341	4.30	0.98	2	374	171	759	190	12	13	12	2.10	0.21	97	1.20
AGAL008.706-00.414	11.68	0.48	2	15356	1267	486	122	0	0	10	0.17	0.75	86	0.00
AGAL008.804-00.327	3.98	0.76	2	315	120	263	66	4	6	8	0.47	0.45	105	0.00
AGAL008.954-00.532	12.84	0.48	1	9264	695	261	65	1	0	8	0.09	1.05	126	4.70
AGAL009.284-00.147	4.22	0.68	2	683	221	401	100	2	3	6	0.60	0.40	99	0.00
AGAL009.851-00.031	2.16	1.44	2	104	140	626	156	61	106	15	2.98	0.18	146	0.00
AGAL009.966-00.021	11.61	0.27	1	2463	113	3054	764	15	12	36	6.62	0.12	86	0.00
AGAL010.404-00.201	2.02	1.44	2	309	441	640	160	10	20	9	1.79	0.23	150	1.21
AGAL010.662-00.156	3.20	1.00	2	164	102	1788	447	29	40	3	11.50	0.09	123	0.00
AGAL010.742-00.126	3.49	0.50	1	781	225	470	117	3	3	7	0.71	0.37	118	2.32
AGAL010.991-00.082	2.92	0.97	2	702	464	300	75	2	2	6	0.38	0.50	129	2.26
AGAL011.004-00.071	3.45	0.50	1	470	137	858	215	15	13	19	2.26	0.21	119	1.09

References. (1) Wienen et al. (2015); (2) Ellsworth-Bowers et al. (2015)

Notes. ^(a) Reid et al. (2009) Galactic rotation parameters.

^(b) Values of $\Sigma_{SFR} < 0.5 \text{ M}_{\odot} \text{ pc}^{-2} \text{ Myr}^{-1}$ are rounded to 0.

^(c) τ_{cross} value equal to 0 implies that there are no available velocity dispersion measurements for this ATLASGAL clump.

Table 4. Properties of resolved, non-star forming ATLASGAL clumps with distance measure

ATLASGAL Name	D ^a	$\sigma(D)$	Ref.	M(H ₂)	$\sigma(M(H_2))$	Σ_{H_2}	$\sigma(\Sigma_{H_2})$	Σ_{SFR}^b	n_{cl}	τ_{ff}	τ_{orb}	τ_{cross}^c
	(kpc)				(M _⊙)	(M _⊙ pc ⁻²)		(M _⊙ pc ⁻² Myr ⁻¹)	(10 ⁴ cm ⁻³)	(Myr)	(Myr)	(Myr)
AGAL005.001+00.086	2.75	1.36	1	127	126	787	197	6	3.81	0.16	133	0.00
AGAL005.387+00.187	2.62	1.32	1	121	122	1217	304	10	7.50	0.11	136	0.28
AGAL005.491-00.441	2.91	1.16	1	245	195	270	68	1	0.55	0.41	129	0.00
AGAL005.852-00.239	2.80	1.14	1	127	103	455	114	4	1.67	0.24	132	0.00
AGAL006.498-00.322	3.27	0.86	1	589	309	489	122	3	0.87	0.33	121	0.00
AGAL006.564-00.319	3.26	0.86	1	361	190	1276	319	11	4.67	0.14	122	0.57
AGAL008.282+00.166	3.06	1.10	2	159	115	435	109	4	1.40	0.26	125	0.00
AGAL008.691-00.401	11.76	0.54	2	17897	1645	1516	379	0	0.86	0.33	88	0.00
AGAL009.038-00.521	4.48	0.70	2	916	285	504	126	1	0.73	0.36	94	2.42
AGAL009.796-00.707	3.53	0.54	1	364	111	688	172	2	1.84	0.23	117	0.00
AGAL009.951-00.366	13.78	1.32	2	8423	1609	464	116	0	0.21	0.67	135	0.00
AGAL009.981-00.386	13.86	1.38	2	5747	1146	1583	396	1	1.62	0.24	137	0.00
AGAL009.999-00.034	11.62	0.27	1	1513	69	1875	469	6	4.06	0.15	86	1.43
AGAL010.004-00.354	13.86	1.23	2	3646	648	1004	251	1	1.03	0.30	137	0.00
AGAL010.079-00.196	1.95	0.88	1	71	64	525	131	7	2.78	0.18	119	0.00
AGAL010.574-00.577	1.19	1.03	1	16	28	2384	596	95	56.73	0.04	207	0.00
AGAL010.659+00.079	2.48	1.43	2	232	268	533	133	2	1.57	0.25	139	0.00
AGAL010.752-00.197	3.24	0.98	2	673	409	571	143	1	1.02	0.30	122	0.00
AGAL010.972-00.094	3.58	0.72	2	639	259	750	187	2	1.58	0.24	115	1.36
AGAL011.001-00.372	1.12	0.98	1	47	82	809	202	11	6.56	0.12	206	0.00

References. (1) Wienen et al. (2015); (2) Ellsworth-Bowers et al. (2015)

Notes. ^(a) Reid et al. (2009) Galactic rotation parameters.

^(b) Σ_{SFR} are 2 σ upper limits.

^(c) τ_{cross} value equal to 0 implies that there are no available velocity dispersion measurements for this ATLASGAL clump.